

# Three-Dimensional Neutron Far-Field Tomography of a Bulk Skyrmion Lattice

M. E. Henderson,<sup>1,2,\*</sup> B. Heacock,<sup>3,†</sup> M. Bleuel,<sup>3</sup> D. G. Cory,<sup>1,4</sup> C. Heikes,<sup>3</sup> M. G. Huber,<sup>3</sup> J. Krzywon,<sup>3</sup> O. Nahman-Levesqué,<sup>1,2</sup> G. M. Luke,<sup>5,6</sup> M. Pula,<sup>5</sup> D. Sarenac,<sup>1</sup> K. Zhernenkov,<sup>1,7</sup> and D. A. Pushin<sup>1,2,‡</sup>

<sup>1</sup>*Institute for Quantum Computing, University of Waterloo, Waterloo, ON, Canada, N2L3G1*

<sup>2</sup>*Department of Physics & Astronomy, University of Waterloo, Waterloo, ON, Canada, N2L3G1*

<sup>3</sup>*National Institute of Standards and Technology, Gaithersburg, Maryland 20899, USA*

<sup>4</sup>*Department of Chemistry, University of Waterloo, Waterloo, ON, Canada, N2L3G1*

<sup>5</sup>*Department of Physics and Astronomy, McMaster University, Hamilton, ON, Canada, L8S 4M1*

<sup>6</sup>*Brockhouse Institute for Materials Research, Hamilton, ON, Canada, L8S 4M1*

<sup>7</sup>*Jülich Centre for Neutron Science at Heinz Maier-Leibnitz Zentrum, Forschungszentrum Jülich GmbH, 85748 Garching, Germany*

(Dated: August 2, 2022)

Skyrmions are topologically-protected spin textures thought to nucleate and annihilate on points of vanishing magnetization, called Bloch points [1–3]. However, owing to a lack of bulk techniques, experimental visualizations of skyrmion lattices and their stabilization through defects in three-dimensions remain elusive. Here, we present a tomographic algorithm applied to a  $\text{Co}_8\text{Zn}_8\text{Mn}_4$  skyrmion lattice host, processing multi-projection small angle neutron scattering measurements to generate mean scattering feature reconstructions (MSFR) of the bulk spin textures. Digital phantoms validated the algorithm; reconstructions of the sample show a disordered skyrmion lattice with a topological saturation of 63 %, exhibiting three-dimensional topological transitions through two different emergent (anti)monopole defect pathways with densities of  $147 \mu\text{m}^{-3}$  and  $21 \mu\text{m}^{-3}$  for branching and segmentation events, respectively. Our techniques produce experimentally-informed visualizations of bulk skyrmion lattice structures and defects, enabling future bulk studies over a wide variety of sample shapes and chemistries, magnetic phases, and external parameters.

Magnetic skyrmions manifest as spin-vortices, whose topological protection drives particle-like properties and condensation into thermodynamically stable phases in an external magnetic field [4–7]. Most commonly observed as 2D structures in metallic materials [8–13], their quantized emergent magnetic flux [1, 4, 14, 15] which characterizes the Berry phase an electron accrues when following the local magnetization adiabatically [16], generates unique transport phenomena [17–19], multiferroic behavior [20], and electric controllability via ultra-low current densities [15, 21]. Such a culmination of features sees skyrmions as promising candidates for next-generation low-power spintronic information-processing and storage devices [22–24].

In three-dimensions, the uniform stacking of the 2D skyrmion spin structure produces skyrmion tubes elon-

gated along the external magnetic field direction, thought to penetrate surface-to-surface [25]. In physical bulk crystal systems at non-zero temperature, a finite density of defects exist, interrupting the skyrmion string propagation [26]. Because the emergent flux that defines skyrmions is quantized, their nucleation and termination is mediated by emergent magnetic charges that must also be quantized [1]. Skyrmion tube segmentation and branching via emergent magnetic monopoles and antimonopoles (denoted  $S^+$ ,  $S^-$ ,  $B^+$ , and  $B^-$ , respectively) are believed to mediate skyrmion topological transitions [27]. Motion of such defects in response to changes in external parameters, such as field or temperature conditions, have been proposed to drive a change in skyrmion topology through in the unwinding of individual skyrmions [26, 27] and the zipping/unzipping of neighboring skyrmion tubes [1, 2, 27]. Since total emergent charge is conserved, skyrmionic transitions can only take place in three-dimensions when emergent (anti)monopoles are either pinned to a material defect or jammed in place and unable to overcome the activation energy required to travel to the material surface or reach an oppositely-charged monopole to annihilate [2, 8, 28].

Examinations of skyrmions using 2D imaging have revealed a myriad of in-plane skyrmion string deformations including elongated structures [1] and bent skyrmion strings which terminate on the surface [3] or form at edges [28], while 3D imaging in confined systems has revealed axial modulation of skyrmion tubes [30]. In all of these instances, the physical systems being probed are subject to constricted geometries by virtue of the thin-plate or needle-shaped samples required by the techniques. This introduces confinement effects, causing the system to exhibit drastically different energetics to those of bulk samples, favoring surface-pinning [31] and edge-interactions [28, 32, 33] which affect skyrmion formation, shape, interactions, dynamics, and stabilization. A recent study [34] confirmed the presence of interrupted and merging-type skyrmion strings in a sparsely populated micrometer sized thin plate needle-shaped sample of  $\text{Mn}_{1.4}\text{Pt}_{0.9}\text{Pd}_{0.4}\text{Sn}$  using scalar magnetic X-ray tomography. The observations, however, are limited to individual skyrmion strings in a sample thickness only a few

\* mehenderson@uwaterloo.ca

† M.E.H. and B.H. contributed equally

‡ dmitry.pushin@uwaterloo.ca

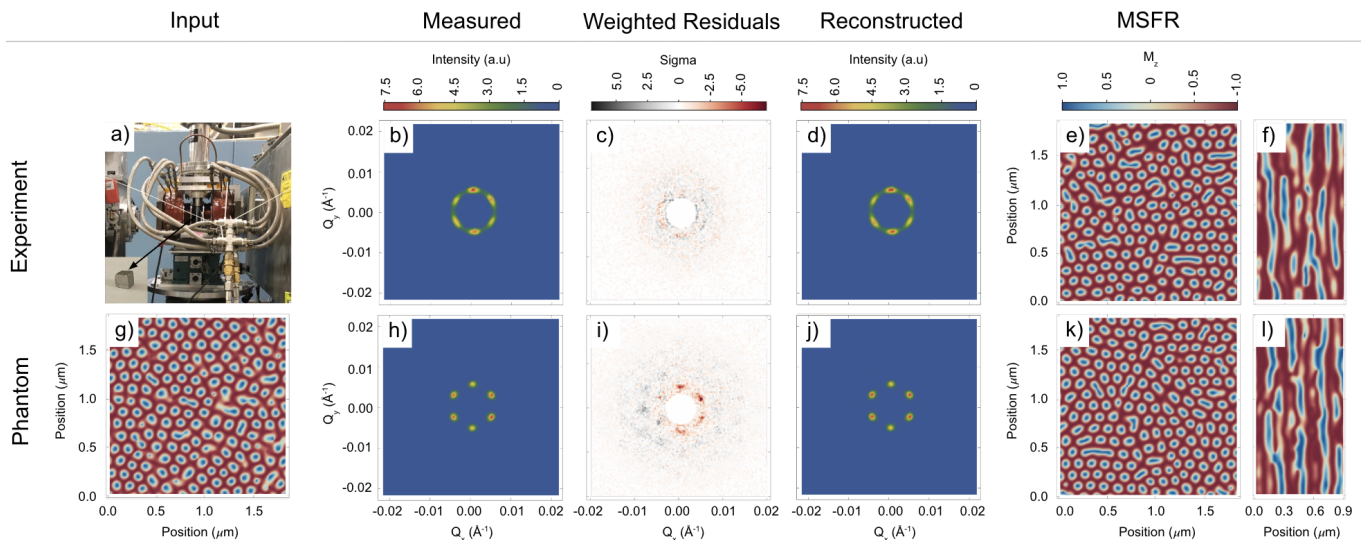


FIG. 1. Experimental setup (a), measured SANS image (b) reproduced from [29], minimized weighted residuals (c), reconstructed SANS image (d), and  $xy$  (e) and  $xz$  (f) slices of the MSFR are shown in the upper panel. The lower panel shows the corresponding plots for the phantoms where (g) is the simulated input magnetization, (h) is the simulation SANS pattern, and (i)-(l) follow the same as the upper experimental row. All SANS images are for the projection with the guide field aligned to the neutron beam.

times the skyrmion tube diameters, whose confined geometry and thickness gradient fundamentally alters the skyrmions shape and behaviour; bulk lattice skyrmion behavior has yet to be experimentally observed.

Small-angle neutron scattering (SANS) is sensitive to bulk scattering features, enabling studies of truly bulk skyrmionic systems along different paths through the sample's phase diagram. In particular, spatially averaged depth information may be obtained by forming rocking curves, integrating over one or more diffraction peaks as a function of sample angle, to extract the longitudinal correlation length of a skyrmion lattice [7]. The effects of recent external magnetic field and temperature history on jammed states has been shown using SANS, where skyrmion lattice defect densities were reduced using an ordering sequence where the external magnetic field is rocked relative to the sample [35].

Whereas previous studies are confined to surface-level techniques, confined systems, or integral far-field SANS measurements which cannot produce real space representations of the sample, here we perform tomography of the thermal equilibrium triangular skyrmion lattice phase using multi-projection SANS measurements coupled with a free energy regularization to generate a three-dimensional mean scattering feature reconstruction of a bulk skyrmion lattice. The reconstruction algorithm consists of first forming an estimator of a multi-projection set of SANS measurements by operating on the incoming neutron state with a forward operator, which takes the MSFR volume as its main input. Next, the sum of weighted residuals between the estimated and measured SANS patterns for multiple projections is minimized with respect to the MSFR. Without integrating over peak ar-

eas before forming the rocking curve, the  $\chi^2$  is sensitive to shifting peak locations, shapes, intensities, and correlations. The number of free parameters depends on the chosen MSFR volume, but will usually be larger than the number of data points in the set of SANS images. The large degeneracy of possible solutions and danger of overfitting the data is overcome by adding a free energy regularizing functional to the objective function  $f = \chi^2 + \beta F$ , where the  $\chi^2$  is the weighted sum of measurement residuals,  $F$  is the free energy of the MSFR, and  $\beta$  is a Lagrange multiplier reminiscent of a Boltzmann factor. The free energy includes the Heisenberg exchange, Dzyaloshinskii-Moriya (DM) exchange, and external field Zeeman terms and could be made to include additional interactions which are functionals of the spin density, though such terms are beyond the scope of the present work. Similar techniques are often used in traditional computed tomography (CT) algorithms, in which case the total variation can be used as a regularizing functional [36]. The resulting MSFRs may be interpreted as containing the types of structures, and their densities, which are common within the sample. However, there is no portion of the sample which looks exactly like a MSFR, and there are a large number of possible MSFRs which would converge on a minimum of the objective function. One can also view minimizing the objective function as performing a micromagnetic simulation with the  $\chi^2$  providing the local interaction and pinning potential terms in the free energy that cause lattice defects, thereby enforcing the lattice correlation lengths and structure encoded in the SANS patterns.

Multi-projection SANS measurements were made using an above room temperature skyrmion host

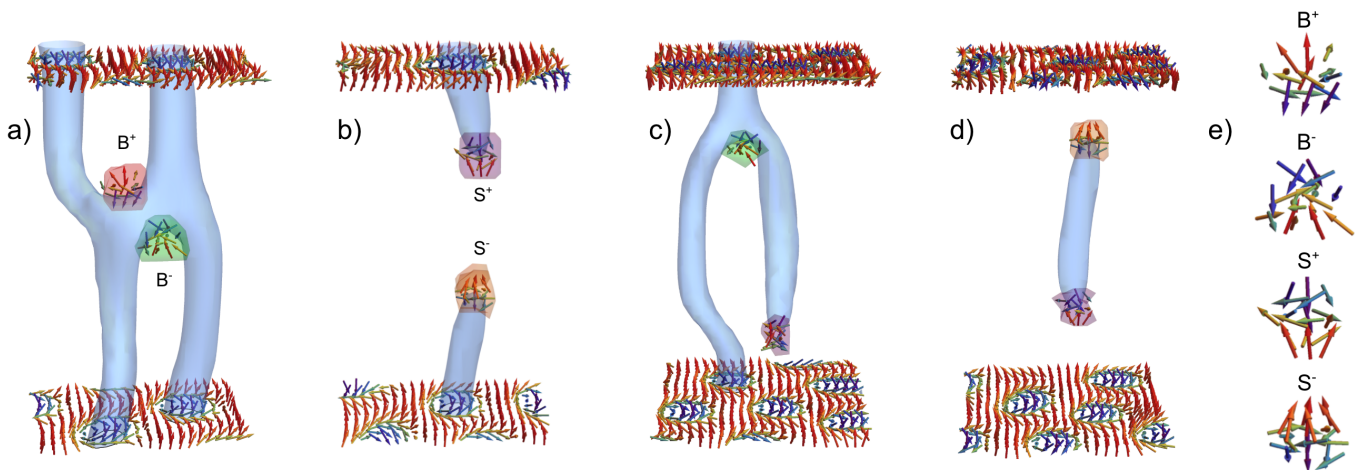


FIG. 2. Characteristic topological transitions present in the MSFR showing branching and segmentation (anti)monopole pathways. The blue contours outline the skyrmion tubes where the out of plane magnetization,  $m_z = -0.5$ . Some of the skyrmion tubes are masked to highlight the regions undergoing changes in topology. Emergent magnetic charge density contours are shown for the two types of skyrmion topological transition processes with  $S^+$ ,  $S^-$ ,  $B^+$ , and  $B^-$  corresponding to purple, orange, red, and green, respectively. Branching (B) and segmentation (S) emergent (anti)monopoles are observed to occur at transition points along the tubes, displaying distinct spin-textures determined by the sign of  $\partial_z m_z$ . Zoomed in spin textures are shown for the labeled branching and segmentation (anti)monopoles with each spin corresponding to one voxel (e). All skyrmion features are shown for a depth of 37 voxels, equating to 531 nm (see materials and methods).

$\text{Co}_8\text{Zn}_8\text{Mn}_4$  previously characterized in [29]. This class of materials has been studied across a variety of techniques including SANS [6, 29, 37–40], magnetic susceptibility [6, 29, 37, 38], and Lorentz Transmission Electron Microscopy (LTEM) [6, 37]. The sample and magnetic field were rotated through 30 projections over a 5.8 degree angular range, which was limited by the geometry of the guide field coils (Fig. 1a). To determine the implications for how a limited-projection dataset would effect our results, we reconstructed digital phantoms under both ideal conditions, where SANS data was simulated for 31 projections between  $\pm 15$  deg about both axes (no compound rotations) and the actual experimental projections (see methods, supplementary materials).

Two-dimensional slices of the measured and reconstructed SANS images, weighted residuals, and MSFRs are shown for the bulk sample and phantom set B with average magnetizations of 0.42 and 0.41, respectively. (Fig. 1). Videos showing magnetization and topological defects as a function of depth for the phantoms and MSFRs are available with the supplementary materials. Average magnetization, topological saturation, and defect densities are compared in Table 1. Phantoms were generated with the external field near the helical-skyrmion boundary (Phantom A), the ideal value (Phantom B), and the ferromagnetic-skyrmion boundary (Phantom C). The required weighting of the Zeeman term  $h$ , to achieve the average magnetization that was estimated from DC-susceptibility, was affected by the  $\chi^2$ . The favored MSFR are thus those with values of  $h$  which produce the estimated average magnetization and are highlighted in Table 1. The agreement between phantom and MSFR is

reasonable for Phantoms B and C. However, the MSFR for Phantom A overestimates the branching defect density. This is likely attributable to the seeding, where Phantom A transitioned from an average magnetization of  $\langle m_z \rangle = 0.4$  to  $\langle m_z \rangle = 0.33$  during the free energy relaxation (see Materials and Methods), while the MSFR had a net magnetization change of  $\langle m_z \rangle = 0.35$  to  $\langle m_z \rangle = 0.32$ , suggesting hysteresis-like effects can impact the fidelity of the reconstructions.

The sample MSFR topological saturation  $N_{\text{sk}}/N_{\text{max}}$  is found to be 63 % of that of a perfect, skyrmion triangular lattice with the same  $Q_0$ . This is reflected by the presence of transverse and longitudinal lattice distortions. In particular, skyrmion voids, bimerons, and elongated spin structures present in the two-dimensional MSFR magnetization slices reduce the number of skyrmions from that of an ideal hexagonally packed lattice. Similarly, interruption of the skyrmion strings along their length may be visualized by taking an  $x - z$  slice of the MSFR as shown in Fig. 1f.

Three-dimensional visualizations of portions of the MSFRs show skyrmion nucleation and annihilation along their depth, where segmentation  $S^\pm$  and branching  $B^\pm$  (anti)monopoles mediate the change in topology at skyrmion transition points (Fig. 2e). These features are similar to those observed for simulations of skyrmion annihilation in three-dimensions through helical and conical pathways [1, 2, 27]. Notably, some branching events are observed to occur along wave vectors  $Q$  which are offset by 60 degrees from the horizontal nearest-neighbor skyrmion, producing a skyrmion twisting effect (Fig. 2a). Conversely, some instances of segmentation events ex-

	$h$	$\langle m_z \rangle_{\text{seed}}$	$\langle m_z \rangle$	$N_{\text{sk}}/N_{\text{max}}$	$\rho_{\text{branch}}, \mu\text{m}^{-3}$	$\rho_{\text{seg}}, \mu\text{m}^{-3}$	$\rho_{\text{tot}}, \mu\text{m}^{-3}$
Phantom A	0.56	0.40	0.33	65 %	101	37	138
MSFR A, ideal	0.50	0.30	0.28	52 %	322	7	329
	0.60	0.35	0.32	59 %	238	13	251
	0.75	0.40	0.37	65 %	150	26	176
MSFR A, lim. proj.	0.50	0.30	0.30	56 %	299	9	308
	0.60	0.35	0.34	60 %	233	13	246
	0.75	0.40	0.40	64 %	164	24	189
Phantom B	0.75	0.40	0.41	68 %	47	40	87
MSFR B, ideal	0.60	0.35	0.35	62 %	138	10	148
	0.75	0.40	0.38	64 %	115	12	127
	0.87	0.45	0.42	72 %	53	31	84
MSFR B, lim. proj.	0.60	0.35	0.35	60 %	166	6	172
	0.75	0.40	0.41	67 %	88	16	104
	0.87	0.45	0.45	69 %	53	31	84
Phantom C	0.94	0.40	0.47	73 %	13	103	115
MSFR C, ideal	0.80	0.42	0.41	69 %	133	27	161
	0.94	0.47	0.46	72 %	54	56	110
	1.08	0.52	0.49	72 %	21	91	112
MSFR C, lim. proj.	0.80	0.42	0.43	69 %	126	26	152
	0.94	0.47	0.49	72 %	46	63	109
	1.08	0.52	0.54	71 %	23	95	119
MSFR, sample	0.50	0.30	0.25	53 %	214	6	220
	0.60	0.35	0.35	59 %	163	13	176
	0.75	0.40	0.42	63 %	118	21	139
	0.87	0.45	0.48	66 %	69	37	106

TABLE I. Zeeman term weight in reduced field units  $h$ , seeded and final average magnetization, topological saturation, and defect densities of the phantoms and associated MSFRs and sample MSFR. The reduced field is fixed; all other parameters are computed from the spin density.

hibit pairs of  $S^\pm$  (anti)monopoles which cup skyrmions, producing spatially localized skyrmion filaments which extend longitudinally over a few lattice periods (Fig. 2d) and are reminiscent of magnetic torons [41]. Given the field history of the sample, wherein saturation to the ferromagnetic phase was performed prior to collection of the tomography data, these structures may represent a skyrmion survival mechanism in the field-polarized state via magnetic torons on defect pinning sites [40]. Future studies will be performed to examine the prevalence of these structures as a function of field history and average magnetization, shedding insight into skyrmion elongation and stabilization mechanisms.

The energy source required for emergent (anti)monopole creation may derive from internal chemical disorder present in the material (such as in

material imperfections or site-disorder [12, 16, 27]), thermal activation [42–44], and the external magnetic field setting relative to the helical and ferromagnetic phase boundaries [1, 3, 43]. For the case of the magnetic field setting, segmentation and branching (anti)monopoles are thought to control skyrmion annihilation upon increasing and decreasing fields, respectively [1, 2, 45]. This is reinforced by reconstructions performed on equivalent datasets under different average magnetization and reduced field  $h$  conditions; a shifting prevalence from branching defects in the low-field case, to segmenting defects in the high-field case is observed.

The preferred sample MSFR shows segmentation and branching (anti)monopoles seemingly jammed in place and unable to travel to the sample surfaces or annihilate. The observed defect densities could be due to

pinning potentials in the material which would trap the (anti)monopoles and inhibit their motion [16]. In this case, the prevalence of these structures may indicate the degree of internal chemical disorder, providing snapshots of magnetic defect pinning centers. Alternatively, these features may be evidence of an incomplete ordering sequence, wherein the limited magnetic field directions during rotation did not allow the monopoles to propagate along enough angular paths in the sample to completely breakup the jammed labyrinth domains [35]. Future SANS tomography measurements taken as a function of skyrmion ordering could decouple these two possibilities. Implementation with structured neutron beams, which possess an analogous non-trivial winding character in spin [46] or phase [47, 48], may provide estimates of the magnetic defect densities based on the vertical widening of the skyrmion peaks in the transverse geometry. Alternatively, the defects themselves may be viewed as the magnetic equivalent of phase singularities, capable of generating topological neutron states for probing nanometric sample topologies.

We have shown experimentally-informed visualizations of a bulk triangular skyrmion lattice, uncovering 3D topological transitions which clearly exhibit a mixture of distinctive segmenting and branching (anti)monopole

defects. Unique features for these two event types are observed in the MSFR, characterized by skyrmion twisting during branching events and localized skyrmion filament structures cupped by  $S^\pm$  (anti)monopoles. Our SANS tomography techniques open the door to future studies of bulk micromagnetic materials on unprecedented length-scales, including skyrmion and emergent (anti)monopole structure, behaviour, and dynamic processes.

## ACKNOWLEDGMENTS

BH would like to thank Dustin Gilbert for suggesting that skyrmion systems would be an interesting subject to study with SANS tomography. This work was supported by the Canadian Excellence Research Chairs (CERC) program, the Natural Sciences and Engineering Council of Canada (NSERC) Discovery program, the Canada First Research Excellence Fund (CFREF), and the National Institute of Standards and Technology (NIST) and the US Department of Energy, Office of Nuclear Physics, under Interagency Agreement 89243019SSC000025. Access to SANS and CHRNS was provided by the Center for High Resolution Neutron Scattering, a partnership between NIST and the National Science Foundation under Agreement No. DMR-1508249.

- 
- [1] P. Milde, D. Köhler, J. Seidel, L. Eng, A. Bauer, A. Chacon, J. Kindervater, S. Mühlbauer, C. Pfleiderer, S. Buhrandt, *et al.*, Unwinding of a skyrmion lattice by magnetic monopoles, *Science* **340**, 1076 (2013).
  - [2] F. Kagawa, H. Oike, W. Koshibae, A. Kikkawa, Y. Okamura, Y. Taguchi, N. Nagaosa, and Y. Tokura, Current-induced viscoelastic topological unwinding of metastable skyrmion strings, *Nature communications* **8**, 1332 (2017).
  - [3] X. Yu, J. Masell, F. S. Yasin, K. Karube, N. Kanazawa, K. Nakajima, T. Nagai, K. Kimoto, W. Koshibae, Y. Taguchi, N. Nagaosa, and Y. Tokura, Real-space observation of topological defects in extended skyrmion-strings, *Nano Letters* **20**, 7313 (2020).
  - [4] N. Nagaosa and Y. Tokura, Topological properties and dynamics of magnetic skyrmions, *Nature nanotechnology* **8**, 899 (2013).
  - [5] S. Mühlbauer, B. Binz, F. Jonietz, C. Pfleiderer, A. Rosch, A. Neubauer, R. Georgii, and P. Böni, Skyrmion lattice in a chiral magnet, *Science* **323**, 915 (2009).
  - [6] Y. Tokunaga, X. Yu, J. White, H. M. Rønnow, D. Morikawa, Y. Taguchi, and Y. Tokura, A new class of chiral materials hosting magnetic skyrmions beyond room temperature, *Nature communications* **6**, 7638 (2015).
  - [7] T. Adams, S. Mühlbauer, C. Pfleiderer, F. Jonietz, A. Bauer, A. Neubauer, R. Georgii, P. Böni, U. Keiderling, K. Everschor, *et al.*, Long-range crystalline nature of the skyrmion lattice in mnsi, *Physical review letters* **107**, 217206 (2011).
  - [8] S. Woo, K. Litzius, B. Krüger, M.-Y. Im, L. Caretta, K. Richter, M. Mann, A. Krone, R. M. Reeve, M. Weigand, *et al.*, Observation of room-temperature magnetic skyrmions and their current-driven dynamics in ultrathin metallic ferromagnets, *Nature materials* **15**, 501 (2016).
  - [9] R. Wiesendanger, Nanoscale magnetic skyrmions in metallic films and multilayers: a new twist for spintronics, *Nature Review Materials* **1**, 16044 (2016).
  - [10] N. S. Kiselev, A. N. Bogdanov, R. Schäfer, and U. K. Röbber, Chiral skyrmions in thin magnetic films: new objects for magnetic storage technologies?, *Journal of Physics D: Applied Physics* **44**, 392001 (2011).
  - [11] X. Z. Yu, N. Kanazawa, Y. Onose, K. Kimoto, W. Z. Zhang, S. Ishiwata, Y. Matsui, and Y. Tokura, Near room-temperature formation of a skyrmion crystal in thin-films of the helimagnet fege, *Nature Materials* **10**, 106 (2011).
  - [12] X. Z. Yu, Y. Onose, N. Kanazawa, J. H. Park, J. H. Han, Y. Matsui, N. Nagaosa, and Y. Tokura, Real-space observation of a two-dimensional skyrmion crystal, *Nature* **465**, 901 (2010).
  - [13] S. Heinze, K. von Bergmann, M. Menzel, J. Brede, A. Kubetzka, R. Wiesendanger, G. Bihlmayer, and S. Blügel, Spontaneous atomic-scale magnetic skyrmion lattice in two dimensions, *Nature Physics* **7**, 713 (2011).
  - [14] T. H. R. Skyrme, A unified field theory of mesons and baryons, *Nuclear Physics* **31**, 556 (1962).
  - [15] T. Schulz, R. Ritz, A. Bauer, M. Halder, M. Wagner, C. Franz, C. Pfleiderer, K. Everschor, M. Garst, and A. Rosch, Emergent electrodynamics of skyrmions in a chiral magnet, *Nature Physics* **8**, 301 (2012).

- [16] C. Schütte and A. Rosch, Dynamics and energetics of emergent magnetic monopoles in chiral magnets, *Physical Review B* **90**, 174432 (2014).
- [17] A. Neubauer, C. Pfleiderer, B. Binz, A. Rosch, R. Ritz, P. G. Niklowitz, and P. Böni, Topological hall effect in the  $a$  phase of mnsi, *Physical Review Letters* **102**, 186602 (2009).
- [18] W. Jiang, X. Zhang, G. Yu, W. Zhang, X. Wang, M. Benjamin Jungfleisch, J. E. Pearson, X. Cheng, O. Heinonen, K. L. Wang, Y. Zhou, A. Hoffmann, and S. G. E. te Velthuis, Direct observation of the skyrmion hall effect, *Nature Physics* **13**, 162 (2017).
- [19] N. Kanazawa, M. Kubota, A. Tsukazaki, Y. Kozuka, K. S. Takahashi, M. Kawasaki, M. Ichikawa, F. Kagawa, and Y. Tokura, Discretized topological hall effect emerging from skyrmions in constricted geometry, *Physical Review B* **91**, 041122 (2015).
- [20] S. Seki, X. Z. Yu, S. Ishiwata, and Y. Tokura, Observation of skyrmions in a multiferroic material, *Science* **336**, 198 (2012).
- [21] F. Jonietz, S. Mühlbauer, C. Pfleiderer, A. Neubauer, W. Münzer, A. Bauer, T. Adams, R. Georgii, P. Böni, R. A. Duine, K. Everschor, M. Garst, and A. Rosch, Spin transfer torques in mnsi at ultralow current densities, *Science* **330**, 1648 (2010).
- [22] X. Zhang, M. Ezawa, and Y. Zhou, Magnetic skyrmion logic gates: conversion, duplication and merging of skyrmions, *Scientific Reports* **5**, 9400 (2015).
- [23] J. Sampaio, V. Cros, S. Rohart, A. Thiaville, and A. Fert, Nucleation, stability and current-induced motion of isolated magnetic skyrmions in nanostructures, *Nature Nanotechnology* **8**, 839 (2013).
- [24] R. Tomasello, E. Martinez, R. Zivieri, L. Torres, M. Carpentieri, and G. Finocchio, A strategy for the design of skyrmion racetrack memories, *Scientific Reports* **4**, 6784 (2014).
- [25] G. van der Laan, S. L. Zhang, and T. Hesjedal, Depth profiling of 3d skyrmion lattices in a chiral magnet—a story with a twist, *AIP Advances* **11**, 015108 (2021).
- [26] J. Iwasaki, M. Mochizuki, and N. Nagaosa, Current-induced skyrmion dynamics in constricted geometries, *Nature Nanotechnology* **8**, 742 (2013).
- [27] M. T. Birch, D. Cortés-Ortuño, N. D. Khanh, S. Seki, A. Štefančič, G. Balakrishnan, Y. Tokura, and P. D. Hatton, Topological defect-mediated skyrmion annihilation in three dimensions, *Communication Physics* **4**, 175 (2021).
- [28] M. Birch, D. Cortés-Ortuño, L. Turnbull, M. Wilson, F. Groß, N. Träger, A. Laurenson, N. Bukin, S. Moody, M. Weigand, *et al.*, Real-space imaging of confined magnetic skyrmion tubes, *Nature communications* **11**, 1 (2020).
- [29] M. E. Henderson, J. Beare, S. Sharma, M. Bleuel, P. Clancy, D. G. Cory, M. G. Huber, C. A. Marjerrison, M. Pula, D. Sarenac, *et al.*, Characterization of a disordered above room temperature skyrmion material  $\text{Co}_8\text{Zn}_8\text{Mn}_4$ , *Materials* **14**, 4689 (2021).
- [30] D. Wolf, S. Schneider, U. K. Röbber, A. Kovács, M. Schmidt, R. E. Dunin-Borkowski, B. Büchner, B. Rellinghaus, and A. Lubk, Unveiling the three-dimensional magnetic texture of skyrmion tubes, *Nature Nanotechnology* **17**, 250 (2022).
- [31] W. Koshibae and N. Nagaosa, Dynamics of skyrmion in disordered chiral magnet of thin film form, *Scientific Reports* **9**, 5111 (2019).
- [32] H. Du, R. Che, L. Kong, X. Zhao, C. Jin, C. Wang, J. Yang, W. Ning, R. Li, C. Jin, X. Chen, J. Zang, Y. Zhang, and M. Tian, Edge-mediated skyrmion chain and its collective dynamics in a confined geometry, *Nature Communications* **6**, 8504 (2015).
- [33] S. A. Meynell, M. N. Wilson, H. Fritzsche, A. N. Bogdanov, and T. L. Monchesky, Surface twist instabilities and skyrmion states in chiral ferromagnets, *Phys. Rev. B* **90**, 014406 (2014).
- [34] S. Seki, M. Suzuki, M. Ishibashi, R. Takaagi, N. D. Khanh, Y. Shiota, K. Shibata, W. Koshibae, Y. Tokura, and T. Onu, Direct visualization of the three-dimensional shape of skyrmion strings in a noncentrosymmetric magnet, *Nature Materials* , 1 (2021).
- [35] D. A. Gilbert, A. J. Grutter, P. M. Neves, G.-J. Shu, G. Zimanyi, B. B. Maranville, F.-C. Chou, K. Krycka, N. P. Butch, S. Huang, *et al.*, Precipitating ordered skyrmion lattices from helical spaghetti and granular powders, *Physical Review Materials* **3**, 014408 (2019).
- [36] E. Y. Sidky and X. Pan, Image reconstruction in circular cone-beam computed tomography by constrained, total-variation minimization, *Physics in Medicine & Biology* **53**, 4777 (2008).
- [37] K. Karube, J. S. White, N. Reynolds, J. L. Gavilano, H. Oike, A. Kikkawa, F. Kagawa, Y. Tokunaga, H. M. Rønnow, Y. Tokura, and Y. Taguchi, Robust metastable skyrmions and their triangular-square lattice structural transition in a high-temperature chiral magnet, *Nature Materials* **15**, 1237 (2016).
- [38] K. Karube, J. S. White, V. Ukleev, C. D. Dewhurst, R. Cubitt, A. Kikkawa, Y. Tokunaga, H. M. Rønnow, Y. Tokura, and Y. Taguchi, Metastable skyrmion lattices governed by magnetic disorder and anisotropy in  $\beta$ -mn-type chiral magnets, *Phys. Rev. B* **102**, 064408 (2020).
- [39] M. Preißinger, K. Karube, D. Ehlers, B. Szegedi, H.-A. Krug von Nidda, J. S. White, V. Ukleev, H. M. Rønnow, Y. Tokunaga, A. Kikkawa, Y. Tokura, Y. Taguchi, and I. Kezsmarki, Vital role of magnetocrystalline anisotropy in cubic chiral skyrmion hosts, *npj Quantum Mater* **6**, 2397–4648 (2021).
- [40] M. Henderson, M. Bleuel, J. Beare, D. Cory, B. Heacock, M. Huber, G. Luke, M. Pula, D. Sarenac, S. Sharma, *et al.*, Skyrmion alignment and pinning effects in a disordered multi-phase skyrmion material  $\text{Co}_8\text{Zn}_8\text{Mn}_4$ , arXiv preprint arXiv:2112.08669 (2021).
- [41] A. O. Leonov and K. Inoue, Homogeneous and heterogeneous nucleation of skyrmions in thin layers of cubic helimagnets, *Phys. Rev. B* **98**, 054404 (2018).
- [42] H. Oike, A. Kikkawa, N. Kanazawa, Y. Taguchi, M. Kawasaki, Y. Tokura, and F. Kagawa, Interplay between topological and thermodynamic stability in a metastable magnetic skyrmion lattice, *Nat. Phys.* **12**, 62 (2016).
- [43] Y. Tokura and N. Kanazawa, Magnetic skyrmion materials, *Chemical Reviews* **121**, 2857 (2021), pMID: 33164494.
- [44] N. Mathur, F. S. Yasin, M. J. Stolt, T. Nagai, K. Kimoto, H. Du, M. Tian, Y. Tokura, X. Yu, and S. Jin, In-plane magnetic field-driven creation and annihilation of magnetic skyrmion strings in nanostructures, *Advanced Functional Materials* **31**, 2008521 (2021).
- [45] F. Zheng, F. N. Rybakov, A. B. Borisov, D. Song, S. Wang, Z. A. Li, H. Du, N. S. Kiselev, J. Caron, A. Ko-

- vac, M. Tian, Y. Zhang, S. Blugel, and R. E. Dunin-Borkowski, Experimental observation of chiral magnetic bobbars in b20-type fege, *Nature Nanotechnology* **13**, 451 (2018).
- [46] D. Sarenac, C. Kapahi, W. Chen, C. W. Clark, D. G. Cory, M. G. Huber, I. Taminiau, K. Zhernenkov, and D. A. Pushin, Generation and detection of spin-orbit coupled neutron beams, *Proceedings of the National Academy of Sciences* **116**, 20328 (2019).
- [47] C. W. Clark, R. Barankov, M. G. Huber, D. G. Cory, and D. A. Pushin, Controlling neutron orbital angular momentum, *Nature* **525**, 504 (2015).
- [48] D. Sarenac, M. E. Henderson, H. Ekinici, C. W. Clark, D. G. Cory, L. Debeer-Schmitt, M. G. Huber, C. Kapahi, and D. A. Pushin, Experimental realization of neutron helical waves, arXiv preprint arXiv:2205.06263 (2022).
- [49] M. Beg, M. Lang, and H. Fangohr, Ubermag: Towards more effective micromagnetic workflows, *IEEE Transactions on Magnetics*, 1 (2021).
- [50] S. R. Kline, Reduction and analysis of sans and usans data using igor pro, *Journal of applied crystallography* **39**, 895 (2006).
- [51] V. F. Sears, *Neutron optics: an introduction to the theory of neutron optical phenomena and their applications*, Vol. 3 (Oxford University Press, USA, 1989).
- [52] E. Balkind, A. Isidori, and M. Eschrig, Magnetic skyrmion lattice by the fourier transform method, *Physical Review B* **99**, 134446 (2019).
- [53] M. J. Donahue and D. G. Porter, Oommf user's guide, version 1.0 (1999).

## MATERIALS AND METHODS

The  $\text{Co}_8\text{Zn}_8\text{Mn}_4$  material was grown via a modified Bridgman technique in a rapid high temperature furnace at McMaster University, cut into a cube of dimensions 3.4 mm x 3.3 mm x 3.0 mm, and oriented such that the (100) direction was coming out of the major face. Details of the sample, as well as single-projection SANS and susceptibility measurements are available elsewhere [29].

Multi-projection, unpolarized SANS was performed at the NG7-30m beamline at the National Institute for Standards and Technology (NIST) for a 15 m beam configuration at a wavelength of 6 Å. The sample was field cooled from 420 K in a field of 250 G to 310 K and the external field was manually rocked back and forth to achieve the observed six-fold pattern [40].

Digital phantoms were made by seeding an LLG relaxation using Ubermag [49] with a high-energy lattice made to have a fixed correlation volume. The LLG relaxation was stopped after ten iterations to retain a reasonable density of defects. The system used the free energy functional

$$E[\mathbf{m}] = -A\mathbf{m} \cdot \nabla^2\mathbf{m} + D\mathbf{m} \cdot (\nabla \times \mathbf{m}) - \mu_0 M_s \mathbf{H} \cdot \mathbf{m}. \quad (1)$$

with exchange stiffness  $A = 10$  pJ/m, Dzyaloshinskii–Moriya constant  $D = 3.93 \times 10^{-3}$  J/m, saturation

magnetization  $M_s = 1 \times 10^6$  A/m, and external field values of  $H = 0.2080$  T,  $0.2780$  T, and  $0.3475$  T for Phantoms A, B, and C, respectively.

The seed was generated by alternating between Fourier-space and real-space constraints. The magnitude of the sample magnetization in Fourier-space is set by desired correlation volume; the real space magnitude of the sample magnetization was constrained to unity everywhere; and the transverse magnetization was set to be in the direction of the curl of the longitudinal magnetization.

SANS patterns were simulated by applying a forward operator to a randomly-selected and randomly-translated one of twenty phantoms made with differing random initialization. The resulting SANS images from repeating this process at least 100 times were averaged to simulate an incoherent neutron source and create the resulting simulated multi-projection SANS data.

The voxel size of the MSFR is determined by the Fourier-space span of the SANS images  $dx = 2\pi/Q_{\text{tot}} = 2\pi/(dQ N)$ . In this experiment  $dx = 14.3$  nm, as determined by the resolution  $dQ = 3.4 \mu\text{m}^{-1}$  and size  $N \times N = 128 \times 128$  of the SANS images. The height of the MSFR was set to 256 voxels, for a total volume of  $1.8 \mu\text{m} \times 1.8 \mu\text{m} \times 3.7 \mu\text{m} = 12.3 \mu\text{m}^3$ .

To compute the reconstructions, the cost function was minimized using a conjugate gradient method. The  $\mathbf{m}^2 = 1$  constraint was enforced by defining search directions in terms of the angular fields  $\Theta = \arcsin(m_z)$  and  $\Phi = \arctan(m_y, m_x)$ . Ten iterations were run with equal weights for all residuals, which can aid in convergence when measurement uncertainties are dominated by counting statistics and there are regions of low count rates. Following the ten iterations, 100 iterations were run with the weights given the measurement uncertainties provided by the SANS reduction software [50]. A maximum weight was introduced for the low-count rate regions to aid in convergence. The resulting average magnetization was found to depend on the weight given to the Zeeman term  $h$ , so reconstructions over a range of  $h$  and starting average magnetization  $\langle m_z \rangle$  were performed (Table 1), with the preferred MSFR being the one that most closely matches the phantom or experimental average magnetization.

Details on the forward propagator, gradient, and defect density calculations are provided in the Supplementary Materials.

## SUPPLEMENTARY MATERIALS

All MSFRs and phantoms listed in Table 1 have accompanying videos that show magnetization and defects as a function of depth which can be found here: [].

### Forward Propagator

The scattering pattern from passing through a single MSFR volume  $S_{Q\theta}$  for some projection  $\theta$  is computed by propagating a neutron wave function through the sample via the time-evolution operator  $\mathcal{U}$

$$S_{Q\theta} = \left| \left\langle Q \left| \mathcal{U} \right| K_\theta \right\rangle \right|^2. \quad (2)$$

Which is estimated using a translation operator along the  $z$ -direction

$$\mathcal{J}_{\theta,dz} = e^{iK_z(\theta,Q)dz} \quad (3)$$

assuming elastic scattering

$$K_z(\theta, Q) = \sqrt{K^2 - (K \sin \theta - Q_x)^2 - Q_y^2}, \quad (4)$$

where  $K$  is the incoming neutron wave number, along with potential the potential  $V_z$  at layer  $z$

$$\mathcal{U}_{\theta,z+dz} = \mathcal{J}_{\theta,dz} [1 - iV_z dz m_n / K_z], \quad (5)$$

where  $m_n$  is the neutron mass, and  $dz$  is the voxel height. The potential from the sample is computed from its resulting magnetic field by applying the characteristic  $-\hat{Q} \times \hat{Q} \times$  operator in Fourier-space [51]

$$\mathbf{B}_s = -4\pi M_s \mathcal{F}^{-1} \left\{ \hat{Q} \times \hat{Q} \times \mathcal{F}[\mathbf{m}] \right\} \quad (6)$$

where  $M_s$  is the saturated magnetization, with  $4\pi M_s = 1900$  G estimated from DC susceptibility measurements taken at 310 K. The potential also includes the external field and operates on a neutron spinor via Pauli matrices

$$V = -\mu_n \boldsymbol{\sigma} \cdot (\mathbf{B}_s + \mathbf{H}_{\text{ext}}). \quad (7)$$

The unpolarized cross section

$$S_{Q,\theta} = \sum_{s,s'} |\langle Q, s' | \mathcal{U} | K_\theta, s \rangle|^2 \quad (8)$$

is then computed by summing over input  $s$  and selected  $s'$  spin states.

Assuming the longitudinal correlation length of the sample is smaller than the reconstruction height, the observed scattering pattern can be estimated by self-convolving the scattering pattern of a single MSFR  $N$  times

$$I_{Q\theta} = \sum_{Q'',Q'} Y_{QQ'} W_{Q'Q''}^\theta \left[ (S^*)^N I_0 \right]_{Q''\theta}, \quad (9)$$

where  $N$  is the ratio of the sample dimension along the propagation direction and the corresponding size of the MSFR. For this sample  $N = 860$ . Because the forward propagator is a function of the projection of the momentum transfer in the  $x - y$  plane  $Q_{xy}$ , the sparse matrix  $W$  shifts the scale of  $Q$  to be horizontal to the propagation axis. The sparse matrix  $Y$  smears out  $Q = K\Omega_Q \simeq K_{\text{avg}}\Omega_Q(1 - \delta\lambda/\lambda)$ , where  $\Omega_Q$  is the scattering angle, over the neutron's incoming wavelength distribution.

### Seeding

The initial guess is formed by first estimating the three-dimensional vector amplitude of the MSFR in Fourier-space  $|\tilde{m}_0|^2$ . This is accomplished by first performing a  $N^{\text{th}}$ -order deconvolution of the scattering signal with itself and the incoming beam profile, which solves for  $I_\theta$

$$I_{\text{meas}} = (I_{\theta^*})^N I_0 \quad (10)$$

with the  $I_\theta$  slices of  $|\tilde{m}|$  for each measured projection unknown. This is accomplished with modified Richardson-Lucy algorithm, which is iterative

$$I_{\theta,i+1} = I_i \left[ \left( \frac{I_{\text{meas}}}{\epsilon + (I_{\theta,i^*})^N I_0} \right) * (I_{\theta,i^*})^{N-1} I_0 \right] \quad (11)$$

where  $\epsilon$  is a small regulator. When  $N$  is large, this can be unstable, and we found it is often helpful to enact this algorithm in stages, with  $I_{\text{meas}}$  deconvolved from  $I_0$ , then performing the deconvolution in  $n$  stages with  $N' = N^{1/n}$ . It can also be helpful to track the error of the deconvolution and stop iterating, or change the regulator size when the error stops decreasing with iteration number.

After deconvolution is complete, the Bragg peaks were fit to a Lorentzian profile with respect to  $Q_z$ . The projection with the incoming beam aligned with the dominant direction of the skyrmion tubes  $I_{\theta=0}$  was then taken as the  $|\tilde{m}|$ -slice at zero  $Q_z$  and expanded along the  $Q_0 = D/J$  sphere, but attenuated according to the fitted Lorentzian with respect to  $Q_z$ . The result is a smooth function with a Lorentzian envelope along  $Q_z$  that preserves the transverse correlation structure of  $I_{\theta=0}$ . All the  $Q > 0$  structure is then scaled and a DC term is introduced to  $\tilde{m}_0$  to generate the expected net sample magnetization  $\langle m \rangle = \tilde{m}(Q = 0)$ .

After forming an estimate of  $|\tilde{m}_0|$ , a guess for  $m$  is generated with an alternating projections algorithm. The vector field of the MSFR  $m$  is iteratively amended according to its constraints in Fourier and real-space. The Fourier-space constraint is given by the magnitude estimated from the deconvolved SANS data  $|\tilde{m}_0|$

$$\tilde{\mathbf{m}}_{i+1} = \tilde{\mathbf{m}}_i \frac{|\tilde{m}_0|}{|\tilde{m}_i|} \quad (12)$$



For the first few iterations, the transverse components of  $\tilde{m}$  are also redefined according to the sign of the DM term and expected curl around  $m_z$

$$\tilde{m}_{xy} = \pm i Q_{yx} \tilde{m}_z. \quad (13)$$

The real space constraint is  $\mathbf{m}^2 = 1$ . However, it can also be beneficial to let  $m$  relax through a few iterations of a free energy minimizer before reapplying Fourier-space constraints. The net result is a guess  $m$  that adheres reasonably-well to the measured SANS projections, while also having a low free energy.

### Minimization

The chosen cost function was

$$f = \chi^2 + \beta \mathcal{F}, \quad (14)$$

where the  $\chi^2$  is the sum of weighted residuals for all the projections

$$\chi^2 = \sum_{Q,\theta} (I_{Q,\theta} - M_{Q,\theta})^2 w_{Q,\theta} \quad (15)$$

and the free energy includes symmetric and antisymmetric exchange terms and a Zeeman term

$$\mathcal{F} = -\frac{1}{2} \mathbf{m} \cdot \nabla^2 \mathbf{m} + Q_0 \mathbf{m} \cdot (\nabla \times \mathbf{m}) - \mathbf{h} \cdot \mathbf{m} \quad (16)$$

where the reduced field  $\mathbf{h} = \mathbf{H} Q_0^2 / J$ , and helical shell radius  $Q_0 = D/J$  is taken from the SANS patterns. The  $\chi^2$  depends on the difference between the measured SANS patterns  $M_{Q,\theta}$  and estimated SANS intensity for each projection  $I_{Q,\theta}$  computed from the MSFR via Eqn 9. The residuals are weighted according to  $w_{Q,\theta} = 1/\sigma_{Q,\theta}^2$ , which is taken from the SANS reduction software [50], with the dominant uncertainty from Poisson counting statistics.

The Lagrange multiplier  $\beta$  acts like a Boltzmann factor. Since the  $\chi^2 \sim \mathcal{O}(\sqrt{N_{Q,\theta}})$ , where  $N_{Q,\theta}$  is the total number of measured SANS pixels over all projections, and the two kinetic terms in  $\mathcal{F} \sim \mathcal{O}(Q_0^2)$ , a reasonable choice is  $\beta = \sqrt{N_{Q,\theta}}/Q_0^2$ . Adjusting the weight of the Zeeman term  $h$  will change the average magnetization  $\langle m_z \rangle$ . A reasonable value of  $h$  can be selected based on studying the behavior of the free energy term in isolation [52]. However, we found that larger values of  $h$  were needed when the  $\chi^2$  was introduced to achieve the same average magnetization, likely because the  $\chi^2$  acts like a kinetic term which further reinforces the helical shell size  $Q_0$ . We therefore chose to study the behavior of the reconstructions over a range of  $h$ , as is shown in Table 1.

The gradient of the free energy term was computed via finite difference methods, similar to OOMMF [53]. The derivative of the  $\chi^2$  necessitates taking the derivative of the forward operator, which results in computing the overlap of the forward-propagating wavefunction  $\psi_\theta$  with a backward-propagating residual wavefunction  $\chi_\theta$  for each projection

$$\frac{\delta}{\delta \mathbf{m}} \chi^2 = i \mu_n M_s m_n dz \sum_{\theta} \frac{1}{K_z} \mathcal{F}^{-1} \left\{ \mathcal{F} \left\{ \text{Im} \left[ \chi_\theta^\dagger \sigma \psi_\theta \right] \right\} \cdot \left( \mathbb{I} - \hat{Q} \hat{Q} \right) \right\}, \quad (17)$$

where  $\mathcal{F}\{\dots\}$  and  $\mathcal{F}^{-1}\{\dots\}$  indicate forward and reverse Fourier transforms, respectively. The wavefunctions are computed by a combination of forward and backward propagation operators

$$\begin{aligned} \psi_\theta &= \langle x | \mathcal{U}_z | K_\theta \rangle \\ \chi_\theta &= \sum_Q \langle x | \mathcal{U}_{z,f}^{-1} | Q \rangle \tilde{\psi}_{f,Q} G_Q \\ G_Q &= 2 \sum_{Q',Q''} Y_{Q,Q'} W_{Q'',Q'} \{ I_0 * [(I - M)w] \}_{Q'',\theta} \end{aligned} \quad (18)$$

where tildes indicate Fourier-space representations; subscript  $f$  denotes the final state; and  $\mathcal{U}_{z,f}^{-1}$  is the backward in time propagator, starting from the final MSFR layer.

### Defect Densities

The emergent magnetic field is computed from the MSFR and its derivatives

$$b_i = \frac{1}{2} \epsilon_{ijk} \mathbf{m} \cdot (\partial_j \mathbf{m} \times \partial_k \mathbf{m}), \quad (19)$$

where  $\epsilon_{ijk}$  is the fully antisymmetric tensor;  $\partial_i \equiv \partial/\partial x_i$ ; and repeated indices are summed over the three space coordinates. Summing  $z$ -component of this field over an area is identified as the skyrmion winding number in the enclosed area, and the emergent magnetic charge density is defined as the source term for the emergent magnetic field

$$4\pi \rho_{\text{em}} = \nabla \cdot \mathbf{b}. \quad (20)$$

A peak-finding algorithm was used to identify local maxima of  $\rho_{\text{em}}^2$  that survive a threshold cut after a Gaussian blurring. The total emergent charge of the defect was then estimated to be the sum of  $\rho_{\text{em}}$  over the neighboring  $\pm 2$  voxels in all directions. Further classification

of branching (two skyrmion events) versus segmentation (single skyrmion events) was accomplished by summing  $\partial_z m_z$  over the same neighborhood. The same or differing signs of the two summations indicate segmentation and branching defects, respectively.